CORE
Metadata, citation and similar papers at core.ac.uk
Provided by Elsevier - Publisher Connector

Crystal structures of substrate binding to *Bacillus subtilis* holo-(acyl carrier protein) synthase reveal a novel trimeric arrangement of molecules resulting in three active sites

Kevin D Parris[1*†], Laura Lin[1†], Amy Tam[1], Rebecca Mathew[1], Jeffrey Hixon[2], Mark Stahl[1], Christian C Fritz[2], Jasbir Seehra[1] and William S Somers[1*]

Background: Holo-(acyl carrier protein) synthase (AcpS), a member of the phosphopantetheinyl transferase superfamily, plays a crucial role in the functional activation of acyl carrier protein (ACP) in the fatty acid biosynthesis pathway. AcpS catalyzes the attachment of the 4′-phosphopantetheinyl moiety of coenzyme A (CoA) to the sidechain of a conserved serine residue on apo-ACP.

Results: We describe here the first crystal structure of a type II ACP from *Bacillus subtilis* in complex with its activator AcpS at 2.3 Å. We also have determined the structures of AcpS alone (at 1.8 Å) and AcpS in complex with CoA (at 1.5 Å). These structures reveal that AcpS exists as a trimer. A catalytic center is located at each of the solvent-exposed interfaces between AcpS molecules. Site-directed mutagenesis studies confirm the importance of trimer formation in AcpS activity.

Conclusions: The active site in AcpS is only formed when two AcpS molecules dimerize. The addition of a third molecule allows for the formation of two additional active sites and also permits a large hydrophobic surface from each molecule of AcpS to be buried in the trimer. The mutations Ile5→Arg, Gln113→Glu and Gln113→Arg show that AcpS is inactive when unable to form a trimer. The co-crystal structures of AcpS–CoA and AcpS–ACP allow us to propose a catalytic mechanism for this class of 4′-phosphopantetheinyl transferases.

Addresses: [1]Biological Chemistry, Wyeth-Ayerst Research, 87 Cambridge Park Drive, Cambridge, MA 02140, USA and [2]Millennium Pharmaceuticals, Inc, 75 Sidney Street, Cambridge, MA 02140, USA.

*Corresponding authors.
E-mail: parrisk@war.wyeth.com
wsomers@genetics.com

†These authors contributed equally to this work.

Key words: acyl carrier protein, coenzyme A, fatty acid biosynthesis, phosphopantetheinyl transferase, three-dimensional structure, X-ray crystallography

Received: **26 April 2000**
Revisions requested: **7 June 2000**
Revisions received: **26 June 2000**
Accepted: **29 June 2000**

Published: **27 July 2000**

Structure 2000, **8**:883–895

0969-2126/00/$ – see front matter
© 2000 Elsevier Science Ltd. All rights reserved.

Introduction

Acyl carrier proteins (ACPs) play important roles in a number of biosynthetic pathways that are dependent upon acyl group transfers [1]. ACPs are predominately associated with the biosynthesis of fatty acids [2,3] but are also utilized in the synthesis of polyketide antibiotics [4,5], non-ribosomal peptides [6,7], and intermediates used in the synthesis of vitamins, such as the protein-bound coenzymes lipoic acid [8] and biotin [9]. The ACP in each of these pathways is composed of 80–100 residues and is either an integrated domain in a larger multifunctional protein (type I) or is a structurally independent protein that is part of a non-aggregated multienzyme system (type II). Type I ACPs are found in mammals, fungi and certain mycobacteria, whereas type II ACPs are utilized by plants and most bacteria. The *Escherichia coli* ACP for fatty acid synthesis has been over-expressed [10], purified [11,12], and the low-resolution solution structure solved using nuclear magnetic resonance (NMR) spectroscopy [13]. The fact that these proteins are essential for the maturation of the organism has led to their investigation as targets for the development of new antimicrobial agents [14–18].

ACPs require post-translational modification for activity. They are converted from an inactive apo form to an active holo form by the transfer of the 4′-phosphopantetheinyl (P-pant) moiety of coenzyme A (CoA) to a conserved serine on the ACP. The β-hydroxyl sidechain of the serine residue serves as a nucleophilic group attacking the pyrophosphate linkage of CoA. Evidence suggests that each synthase that is dependent upon P-pant attachment for activation has its own partner enzyme responsible for this attachment [19].

The post-translational modification of the ACP subunit in the fatty acid synthase is performed by holo-(acyl carrier protein) synthase (AcpS; EC 2.7.8.7). One of the best-characterized members of the P-pant transferase family is the *E. coli* AcpS [20]. This enzyme produces holo-ACP by transferring the P-pant moiety from CoA to Ser36 of the *E. coli* apo-ACP in a magnesium-dependent reaction [20]. The over-expression and purification of the *E. coli* AcpS has been described [21] and this protein has been classified as a member of a new enzyme superfamily, the phosphopantetheinyl transferases [19]. The P-pant transferase superfamily can be roughly divided into two subgroups

[22]. Enzymes responsible for modifying the peptidyl carrier protein subunits of non-ribosomal peptide synthetases are good examples for the first subgroup, which are usually ~230 amino acids in size. The crystal structure of one member of this enzyme subgroup, the surfactin synthetase activating enzyme Sfp, has been solved recently; the structure has twofold intramolecular pseudosymmetry with the CoA-binding site at the interface of the symmetrical fold [22]. AcpS and other enzymes transferring the P-pant group onto domains of the fatty acid synthases are usually smaller, in the order of 120 residues, and belong to the second subgroup of the P-pant transferase superfamily. The sequence homology between these two subgroups is rather low (between 12 and 22%). Alignment [19–22] of these proteins shows that two regions, residues 5–13 and 54–65 (*E. coli* AcpS numbering), are highly conserved.

Here we report the X-ray crystal structures of *Bacillus subtilis* AcpS both with (at 1.5 Å) and without (at 1.8 Å) bound CoA. Furthermore, we report the structure of AcpS in complex with holo-ACP at 2.3 Å. These structures are the first from the AcpS subfamily of P-pant transferases and the structure of holo-ACP is the first X-ray structure of an ACP. Examination of these structures reveal that each AcpS adopts a fold similar to half of the Sfp molecule with, at a cursory glance, the oligomeric state being the most significant difference between AcpS and Sfp. It has been speculated that the active form of AcpS is a dimer [21,22], but our results show that AcpS forms a trimer that contains three active sites. In this family of enzymes the active site is highly conserved, therefore, the structures detailed here will assist in the design of broad-spectrum antibiotics. Additionally, these structures demonstrate the nature of ACP and CoA binding as well as providing insights into the mechanism of P-pant transfer.

Results and discussion

Structure determination

The crystal structure of AcpS was solved using multiwavelength anomalous diffraction (MAD) with a selenomethionine (SeMet) derivative [23]. Experimental phases were determined at 2.5 Å, modified by solvent-flattening, non-crystallographic symmetry averaging and extended to 2.2 Å. Figure 1 shows that the resulting experimental map

Figure 1

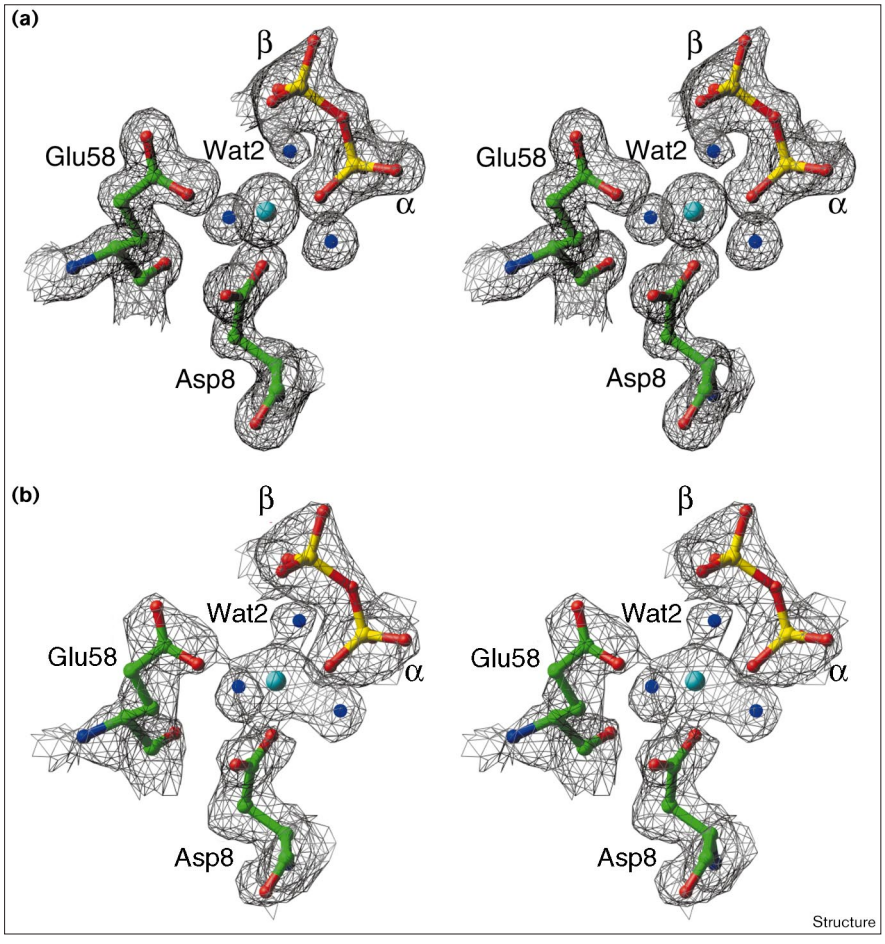

Electron-density maps. **(a)** Experimental map generated with MAD phases, obtained from scattering of selenium in the $P2_1$ form of AcpS, superimposed on the refined coordinates. **(b)** The final refined $2F_o–F_c$ map contoured at 1σ for the same region shown in (a). In both (a) and (b), it is clear that the β-phosphate has trigonal bi-pyramidal characteristics. In addition to the labeled residues, the calcium is shown as a light blue sphere and the waters completing the coordination sphere are in dark blue. The figure was generated with Ribbons [41].

Table 1

Statistics for data collection and phase determination.

	AcpS MAD			AcpS–CoA MAD			AcpS	AcpS–CoA	AcpS–ACP
	Remote	Peak	Inflection	Remote	Peak	Inflection	Native	Native	Native
Wavelength (Å)	λ3 = 0.93	λ1 = 0.97853	λ2 = 0.97860	λ3 = 0.93	λ1 = 0.97836	λ2 = 0.97858	λ = 1.2	λ = 1.2	λ = 1.54
Resolution range (Å)	15–2.4	15–2.5	15–2.4	15–1.9	15–1.9	15–1.9	20–1.8	100–1.5	15–2.3
R_{merge}* (%)	8.0 (25.8)	6.8 (15.5)	7.8 (29.4)	6.0 (36.1)	5.9 (21.4)	5.7 (20.5)	7.6 (46.8)	6.4 (30.7)	5.7 (56.0)
Completeness (%)	100 (100)	100 (100)	100 (100)	99.9 (100)	99.9 (100)	99.6 (100)	96.4 (68.6)	99.9 (98.9)	97.7 (94.5)
Total reflections	239,608	261,205	249,873	62,649	60,726	56,988	31,4385	64,434	27,0151
Unique reflections	38,299	33,941	38,335	8174	6982	7031	87,902	17,170	29,694
I/σ(I)	26.1 (7.03)	31.9 (12.7)	28.4 (8.1)	33.2 (13.1)	36.9 (16.9)	35.8 (16.7)	15.1 (1.9)	18.1 (4.0)	26.6 (3.5)
f′(e^-)†	−2.18	−7.35	−9.5	−2.18	−7.35	−9.52			
f″(e^-)	3.46	5.92	3.15	3.46	5.92	3.15			
MAD phasing: AcpS									
Resolution limits (Å)	6.46	4.8	3.99	3.49	3.13	2.87	2.67	2.5	Overall
Phasing power‡									
λ3 anomalous	2.88	2.01	1.39	1.03	0.8	0.59	0.46	0.35	0.93
λ1 isomorphous	0.003	0.003	0.003	0.003	0.003	1.86	1.48	1.2	0.003
λ1 anomalous	3.85	3.10	2.09	1.59	1.29	1.01	0.80	0.64	1.45
λ2 isomorphous	6.96	5.15	3.34	2.54	2.03	1.64	1.25	0.03	2.19
λ2 anomalous	2.37	1.81	1.28	1.00	0.77	0.60	0.46	0.01	0.80
Mean FOM§	0.77	0.71	0.58	0.48	0.39	0.29	0.21	0.15	0.38
MAD phasing: AcpS–CoA									
Resolution limits (Å)	6.73	4.41	3.50	2.99	2.64	2.40	2.21	2.06	Overall
Phasing power									
λ3 anomalous	3.50	2.50	1.99	1.83	1.42	1.14	0.83	0.66	1.42
λ1 isomorphous	1.57	1.22	1.11	1.16	1.12	1.11	1.01	0.92	1.10
λ1 anomalous	4.54	3.42	2.87	2.64	2.11	1.61	1.22	0.97	2.04
λ2 isomorphous	1.53	1.00	0.67	0.53	0.45	0.36	0.37	0.24	0.51
λ2 anomalous	2.81	2.29	1.98	1.70	1.40	1.14	0.85	0.68	1.37
Mean FOM	0.62	0.51	0.51	0.50	0.44	0.38	0.28	0.12	0.38

*$R_{merge} = \Sigma|I_h - \langle I_h \rangle|/\Sigma I_h$, where $\langle I_h \rangle$ is the average intensity over symmetry equivalents. Numbers in parentheses reflect statistics for the last shell. †f′ and f″ reported values were refined by SHARP. ‡Phasing power $= \Sigma|F_H|/\Sigma||F_{PHobs}| - |F_{PHcalc}||$, where F_H is the calculated heavy-atom structure-factor amplitude. §Figure of merit $= \langle \Sigma P(\alpha) e^{i\alpha} / \Sigma |P(\alpha)| \rangle$, where α is the phase and P(α) is the phase probability distribution.

was of high quality. The final model was refined to a crystallographic R factor of 19.6% and an R_{free} of 21.9% (Tables 1 and 2). Incubating the protein with CoA prior to crystallization generated the complex between AcpS and CoA. The structure of this complex was solved using a combination of molecular replacement and MAD phasing.

Table 2

Refinement statistics.

Model refinement	AcpS	AcpS–CoA	AcpS–ACP
Maximum resolution (Å)	1.8	1.5	2.3
R_{work} (%)*	19.6	18.6	22.2
R_{free} (%)†	21.9	20.1	27.9
<B value> (Å^3)	30.6	17.5	52.3
Rms deviations from ideal geometry			
bonds (Å)	0.007	0.008	0.015
angles (°)	1.34	1.31	1.8
B values (Å^2)	2.18	2.19	2.05
Non-hydrogen protein atoms	6972	1147	6972
Water molecules	471	99	125
Ions	8 Sodium, 19 chlorine	2 Calcium	1 Sodium
Other molecules	5 DTT, 2 glycerol	1 CoA	None

*$R_{work} = \Sigma||F_{obs}| - |F_{calc}||/\Sigma|F_{obs}|$. †$R_{free}$ is equivalent to R_{work}, but calculated for a randomly chosen 5% (or 10%) of reflections omitted from the refinement process.

Figure 2

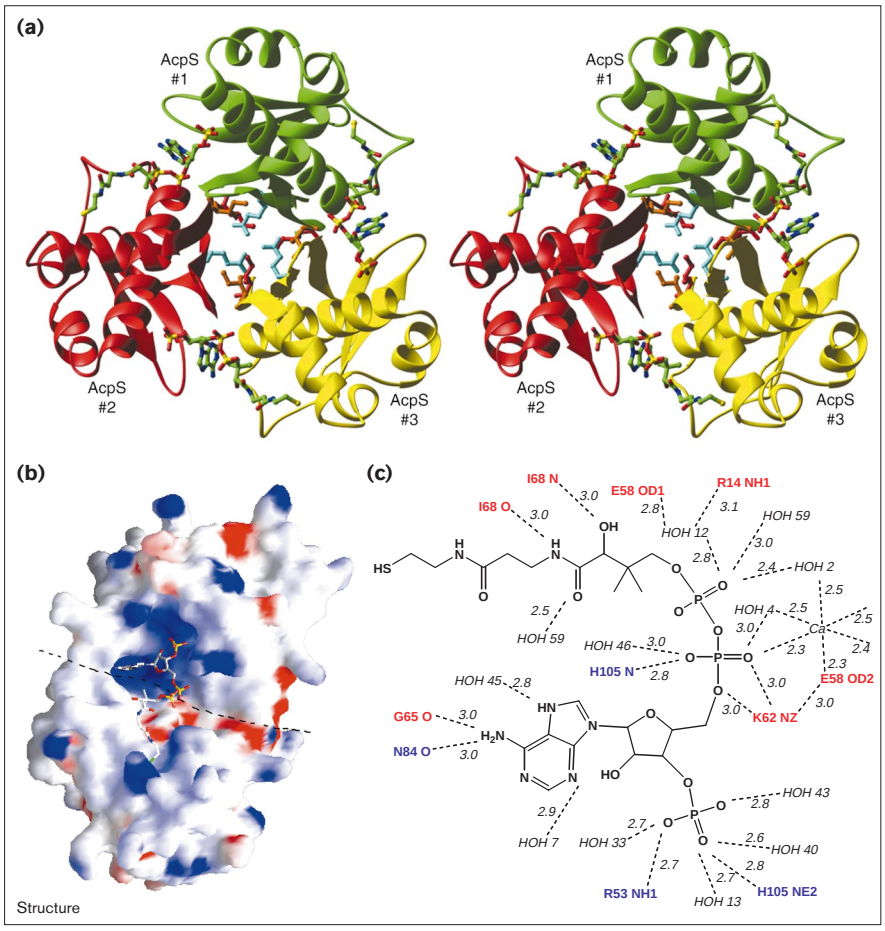

AcpS–CoA interactions. **(a)** Ribbon diagram showing CoA bound in each active site of the AcpS trimer. Also shown in the center of the trimer are the three amino acids chosen for mutagenesis studies: Ile2 (red), Ile5 (brown), Gln113 (blue). This trimeric arrangement of AcpS molecules is observed in all three structures presented in this paper. **(b)** Surface potential representation of the cavity found in the AcpS structures into which CoA and ACP bind. This figure shows how CoA fits into the cavity. The dashed line approximately delineates the boundary between two AcpS molecules. **(c)** Details of the interaction between AcpS, coenzyme A and solvent. Because the active site of this enzyme is composed of two molecules of AcpS those residues that come from one molecule of AcpS are in red and those from the second molecule are in blue. The ribbon diagram was generated with Ribbons [41], the surface potential with GRASP [42], and the distance diagram with ChemDraw CambridgeSoft Corp, Cambridge, MA.

The final model was refined to a crystallographic R factor of 18.6% and an R_{free} of 20.1%. The AcpS protein that was used for crystallizing both the native and CoA complex was recombinant full-length AcpS containing an N-terminal His_6-tag with a glycine spacer. This protein also had a mutation at residue 96, where glutamine was replaced with proline, presumably as a result of an error in the polymerase chain reaction. The activity of this mutant is indistinguishable from the wild-type in its P-pant transferase activity (data not shown).

The structure of the complex between AcpS and holo-ACP was solved with molecular replacement using AMoRe [24] with AcpS from the AcpS–CoA structure as the probe. The final model was refined to a crystallographic R factor of 22.2% and an R_{free} of 27.9%. Holo-ACP was used for the crystallization of this complex and this ACP construct had five additional residues at the N terminus that were a remnant of the protease cleavage site from the glutathione-S-transferase (GST)–ACP fusion protein. The AcpS construct used in obtaining this structure began at residue 2 and did not contain a His_6-tag.

Despite numerous attempts, we were unable to obtain diffraction-quality crystals of the ACP–AcpS complex with the His_6-tagged construct of AcpS used for the native and CoA structures. As a result, we investigated different forms of the protein which ultimately led to the construct used in this co-structure with ACP. This construct of AcpS was a recombinant non-His-tagged protein in which residue 2 was changed from isoleucine to alanine to accommodate a restriction site during plasmid construction. Consequently, the N-terminal initiation methionine was removed during expression in *E. coli* in accordance with the known substrate specificity of *E. coli* methionylaminopeptidase [25]. We were surprised that the activities of these two enzyme constructs were very different but, as we will show, the crystal structures help us interpret this result.

The structure of AcpS

The final model of AcpS contains six copies of the protein arranged as two groups of three (Figure 2). Each copy consists of at least residues 1–118 (Figure 3). Also present in the asymmetric unit are 471 solvent molecules, eight sodium

Figure 3

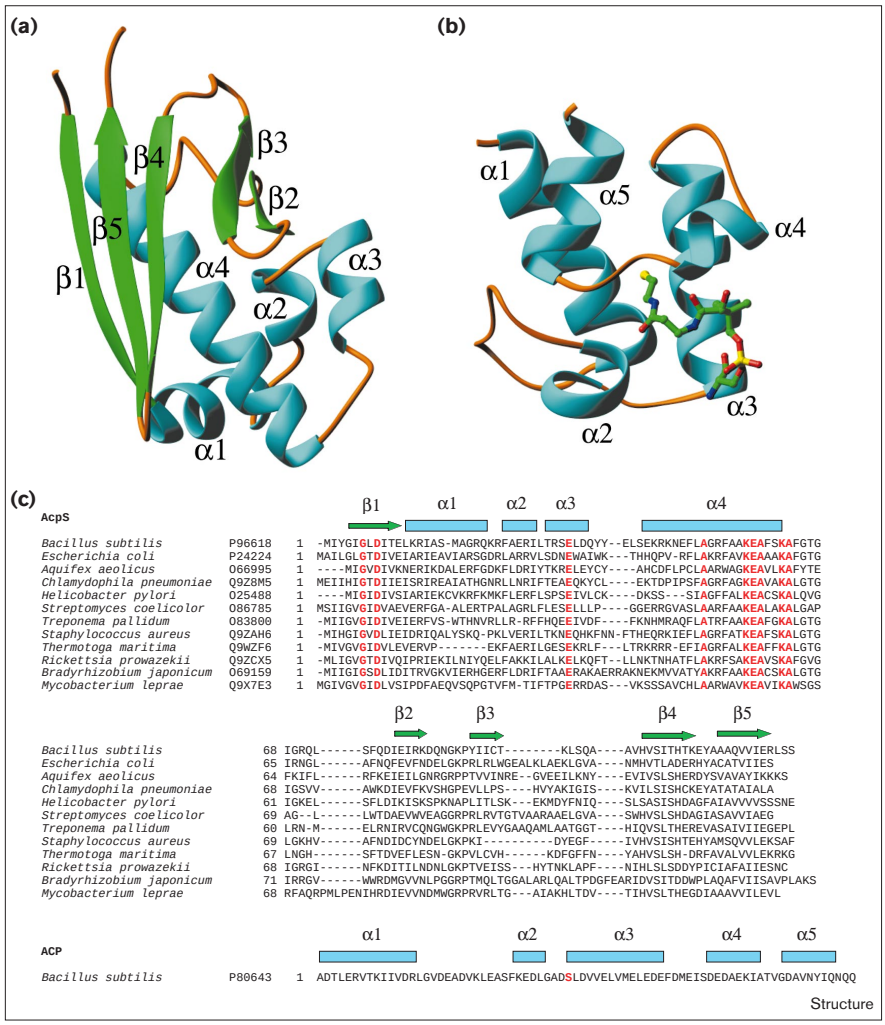

Sequence and secondary structure elements for AcpS and ACP. Ribbon diagram with the secondary structure elements labeled for **(a)** one AcpS molecule and **(b)** an ACP molecule. **(c)** Sequence alignment of 12 AcpS-type P-pant transferases. The conserved residues are shown in red. The secondary structure assignments for *B. subtilis* AcpS are shown above the sequences: helices are shown as rectangles and β strands as arrows. The last 56 residues of *Thermotoga maritima* were omitted as they have no counterpart in the other enzymes. The SWISS-PROT accession numbers are given in the second column for each protein. **(d)** The sequence of *B. subtilis* ACP with the secondary structure elements shown above. The conserved serine to which the P-pant moiety is transferred is shown in red. The ribbon diagrams were generated with Ribbons [41] and the sequence alignment was generated using Microsoft Word.

atoms and 19 chloride ions. The core of the protein is an α helix (α4), composed of residues 43–64, that runs the entire length of the protein. One side of this helix is covered by an antiparallel β sheet (A-sheet) with topology β1, β5 and β4. A β ribbon composed of strands β3 and β2, along with α3 combines to cover another side of helix α4. The encasement of α4 is completed by α1, α2 and a loop consisting of residues 66–75. The fold of this family of proteins is novel, as previously reported [22]. The Cα atoms of the six AcpS molecules in the asymmetric unit can be superimposed with a root mean square difference (rmsd) of 0.497 Å. This alignment is improved to 0.168 Å when three mobile loops (15–24, 80–88, 91–99), the positioning of which differs due to contacts with symmetry-related molecules, are omitted. In monomers 2 and 4, the glycine preceding the His_6-tag is observed but the remainder of the His_6-tag is disordered. The electron density for monomers 2–5 ends at residue 118, whereas that for monomer 1 extends to residue 119 and that for monomer 6 is traceable to residue 120.

Based on the structure of Sfp, Reuter and colleagues [22] postulated that the short-chain P-pant transferases such as AcpS would fold in a similar manner to one half of the Sfp protein, and that they would dimerize in a fashion suggested by the two domains of Sfp. This model was accurate but what was not envisioned was that the AcpS molecules would pack as a trimer, as we show here. Where the Sfp protein has a C-terminal extension that closes off the face opposite the two β sheets, the short-chain P-pant transferases use a third protein molecule. The formation of this trimer buries the 527 ^{3} surface of the A-sheet from each AcpS molecule. Each A-sheet is composed of 27 amino acids. For each molecule of AcpS, the sidechains of 15 residues point in towards the middle of the barrel—six of these residues are hydrophobic. Examination of the face of each β sheet shows that these six hydrophobic residues are located on strands β1 and β5 that are located in the center and to one side of each β sheet. The sidechains from the third strand, β4, that are directed towards the

center of the barrel are all hydrophilic (His100, Ser102, Thr104 and Thr106). The sidechains of these β sheets that are directed away from the center of the barrel possess an electronic nature that compliments those pointing into the barrel; those residues from strand β4 that are pointing away from the barrel are composed mostly of hydrophobic residues while those from strand β1 are composed mostly of hydrophilic residues. This differentiation in hydrogen-bonding ability undoubtedly aids in the orientation and packing of the AcpS molecules to form the active oligomer as the polar sidechains on strand β4 interact with the polar side of strand β1 from a second AcpS molecule. The interface, where the β sheets of two AcpS molecules intersect in the trimer, is therefore polar. The area above this intersection is open to solvent and is at the bottom of a bowl-shaped depression in the surface of the protein assembly. In this structure, the three bowl-shaped depressions are filled with numerous water molecules as well as three chloride ions and one sodium ion. An enzymatic active site is located inside each depression. One half of each active site comes from one molecule of AcpS and the other half from a second AcpS molecule in the trimer. Examination of a surface representation of this depression (Figure 2) shows that it has distinct regions of positive and negative electrostatic potential to aid in cofactor and substrate binding. Aside from the packing of the β sheets, the only other interactions (both van der Waals and ionic) between the three molecules in the trimer occur between residues of two loops consisting of residues 65–67 from one AcpS molecule and residues 84–86 from a second AcpS molecule. The structure of the AcpS trimer was searched against a database of known structures using DALI [26] and the results indicated that there are no known structures with the nine-stranded threefold symmetric pseudo β-barrel motif observed in this oligomer.

The structure of AcpS and CoA

The final model of AcpS–CoA in the rhombohedral crystal contains residues 1–118 of one molecule of AcpS, one molecule of CoA, 99 solvent molecules, two calcium atoms, and one chloride ion. Similar to the AcpS structure described above, the electron density extends to residue 118 and there are no breaks in the density between residues 1–118. The binding of CoA does not result in any changes in the secondary structure of the protein and the same trimeric arrangement of the protein molecules described in the $P2_1$ space group above is also present in this structure (Figure 2). The monomer of AcpS in this structure of the AcpS–CoA complex is positioned such that the molecular threefold axis of the trimer is coincident with a crystallographic threefold axis.

Inside the bowl-shaped depression described above, CoA fits into a groove along the anionic ridge between the A-sheets of two AcpS molecules. The adenine ring of CoA (Figure 2) fits into a pocket formed by a loop consisting of residues 80–88 and residues 62–70 from a symmetry-related molecule. As observed in the structure of CoA bound to Sfp [22], the ribose is present in the 3′-*endo* conformation that has the 2′-hydroxyl placed axially and the 3′-phosphate in an equatorial position. The 3′-phosphate of CoA is held in place by the protein through hydrogen bonds provided by the sidechains of Arg53 and His105 (Figure 2). The interactions between the pantetheine arm and the protein are predominately van der Waals. The β-mercaptoethylamine segment rests in a shallow hydrophobic pocket formed on the surface of the protein by the aliphatic portion of the sidechains of Arg28, Met18, Phe25, Ile29, Phe54 and Phe74. The β-phosphate from the pyrophosphate moiety of CoA has no direct contact with the protein and the α-phosphate is within hydrogen-bonding distance of the mainchain amide of His105 and the ζ-amino group of Lys62. The interactions described here create a mode of binding for the CoA where the pantetheinyl arm extends away from the adenine base (Figure 2). In contrast, the mode of CoA binding in other protein–CoA complexes, such as the human PCAF transcriptional regulator [27], has the pantetheinyl arm bending back toward the adenine base.

The α-phosphate from CoA, along with Glu58 and Asp8 from AcpS, are involved in the coordination of a metal ion; the coordination sphere is completed by three water molecules. This cation is normally magnesium [28] but the bond lengths between this metal ion and its ligands suggest that in this crystal the divalent cation is calcium. This is consistent with the conditions used to obtain these crystals, which have 100 times more calcium than magnesium. We have found (data not shown) that when the protein is subjected to extensive dialysis to remove magnesium and the activity of the enzyme is measured in the presence of calcium, transfer of the P-pant group to ACP still occurs although at a reduced rate.

Sequence alignment of the P-pant transferase family (Figure 3) identified a number of conserved residues [19–22]. In this structure, these residues (Gly6, Asp8, Phe54, Lys57, Glu58, Ala59, Lys62) are all located in the bowl-shaped depression created by two AcpS molecules as described above. This crystal structure of CoA complexed to AcpS allows us to assign a function to these conserved residues. As mentioned above, Asp8 and Glu58 are essential as they both chelate the magnesium ion. Phe54 participates in creating a hydrophobic pocket for the panthetheine arm to rest in as well as restricting the rotational isomers available to the sidechain of Glu58. The mobility of Phe54 is restricted by the location of Lys57 and this residue is held in place via a salt bridge with Glu34. Glu34 was not identified as conserved by Lambalot or Reuter but Figure 3 shows that it is conserved in at least a subset of this family. One of the more intriguing residues in this short list of highly conserved residues is Lys62. This

Figure 4

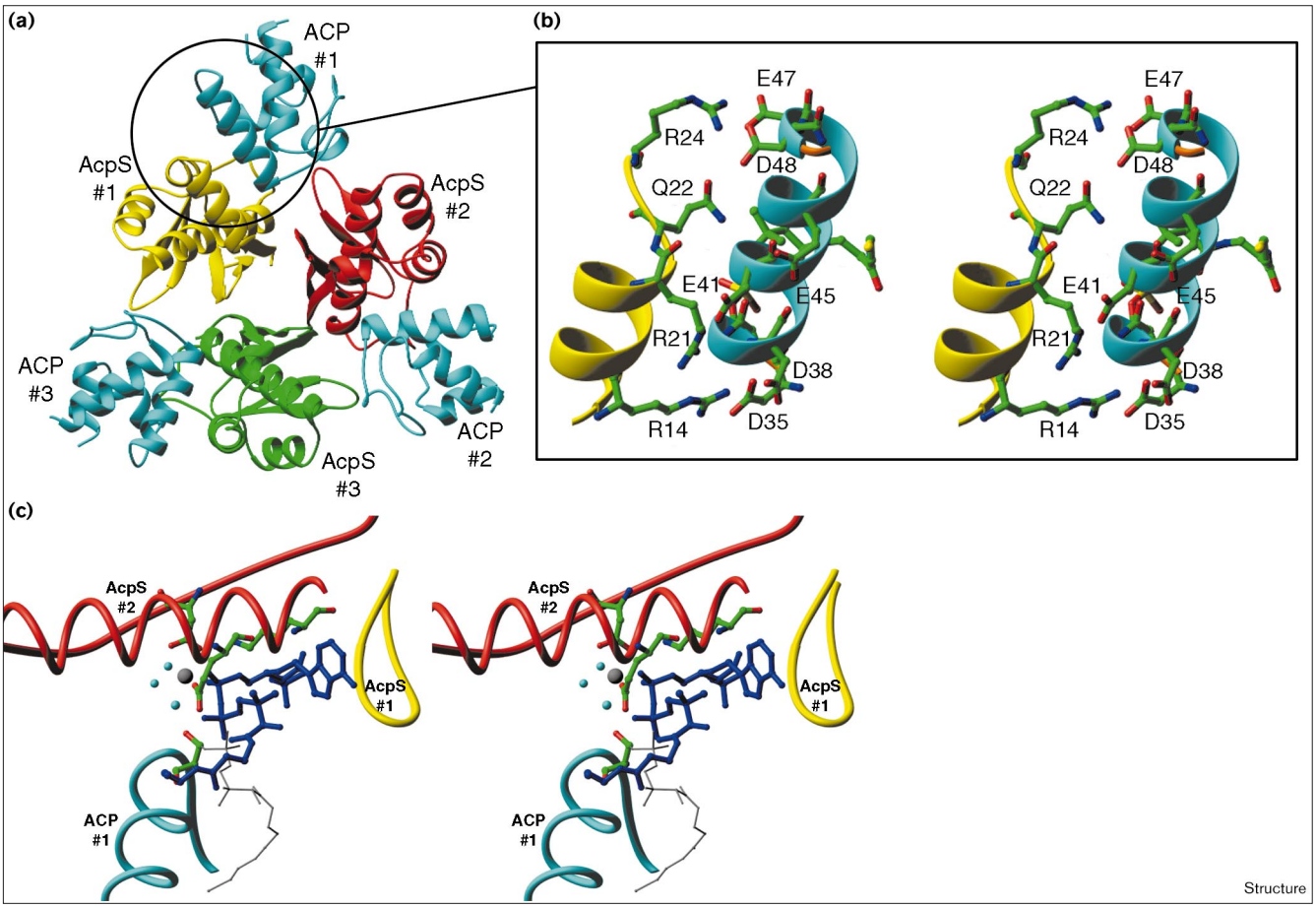

Stereoviews detailing the interaction of ACP and AcpS. **(a)** Ribbon diagram showing ACP bound in each active site of the AcpS trimer. **(b)** View of the interaction between helix α3 of ACP and helix α1 of AcpS. **(c)** When the AcpS molecules as found in the complex structure with CoA are superimposed with the coordinates of AcpS as found in the complex structure with ACP, it is possible to generate a model of AcpS (red and yellow), ACP (light blue) and CoA (dark blue) all binding at the same time. In this illustration the dipole of helix α3 points at the pyrophosphate moiety of CoA placing Ser36 near the β-phosphate and adjacent to a water molecule (Wat2). The conformation of the P-pant group after attachment to Ser36 is shown as a thin gray line. The figure was generated with Ribbons [41].

lies in an extended conformation pointing towards the pyrophosphate moiety of the CoA. It is within hydrogen-bonding distance of the α-phosphate and also Asp8. This positioning suggests a mechanistic role that will be discussed later. As reported by Reuter, the requirement for residues with small sidechains at residues 6 and 59 is owing to spatial considerations. A small sidechain is required at residue 6 as a larger sidechain would interfere with the placement of Lys62 and Ser102. Likewise, a larger sidechain at residue 59 would interfere with the packing between helix α4 and strands β1 and β5 of the A-sheet.

The structures of AcpS and holo-ACP

The final model of AcpS–ACP contains residues 2–118 of AcpS, residues 1–73 of holo-ACP and 117 solvent molecules. The contacts between holo-ACP and AcpS are predominately hydrophilic in nature with almost all of the interactions occurring between helix α1 of AcpS and helix α3 of ACP (Figure 4). There are only two significant hydrophobic contacts and these both involve residues from ACP (Leu37 and Met44) that protrude into hydrophobic pockets on AcpS. Leu37 extends into a pocket formed by Met18, Phe25, Phe54 and Ile15 on AcpS, whereas Met44 binds in a pocket formed by Phe25 and the aliphatic portion of the sidechains from Arg28 and Gln22. These interactions are summarized in Table 3.

Examination of this structure suggests that a key residue in the binding of ACP to AcpS is Arg14 from AcpS. Arg14 forms a salt bridge with the residue just before the reactive serine (Asp35) of ACP and is involved in hydrogen bonding with Asp38, two residues after the reactive serine. These interactions serve to position the ACP molecule so that one end of helix α3 from ACP is placed at

Table 3

Hydrophilic interactions between ACP and AcpS.

ACP residue	AcpS residue	Distance (Å)
Asp35 OD1	Arg214 NH2	2.8
Asp35 OD2	Arg214 NH1	2.5
Asp35 OD2	Arg214 NH2	3.0
Asp38 OD1	Arg214 NH2	3.0
Asp38 OD2	Arg214 NH2	3.2
Glu41 OE1	Arg221 NH2	2.7
Glu41 OE2	Arg221 NE	2.9
Asp48 OD1	Arg224 NH1	2.9
Ile54 O	Arg228 NH2	2.6
Asp56 OD2	Ser273 OG	2.5
Asp56 OD2	Phe274 N	2.8
Glu60 OE2	Ala270 N	3.0

the bottom of the active site and correctly orients Ser36. As shown in Figure 3, Arg14 is conserved in all AcpS proteins, except that from *Mycobacterium* in which it is an aspartic acid. Another arginine residue, Arg21, of AcpS forms a salt bridge with Glu41 from ACP. The other end of helix α3 is positioned by the interactions of Arg24 and Gln22 from AcpS with Asp48 of ACP. These interactions, along with the two hydrophobic 'keys' described above, lock the α3 helix of ACP into place.

When the structure of AcpS–CoA and AcpS–ACP are superimposed it is evident that a loop consisting of residues 64–78 enlarges the active site by shifting 2 Å to accommodate helix α4 from ACP. Additionally, this superimposition of the structures allows for the construction of a model depicting the interaction between AcpS, ACP and CoA (Figure 4). From this model, it can be seen that the dipole of the α2 helix of ACP is directed at the phosphate of the CoA that is to be transferred to ACP.

Mutational analysis of the trimerization domain

To address the question of whether or not the trimer is a physiologically relevant form of AcpS, we carried out mutational studies. As mentioned previously, the driving force of the trimer formation seems to be burying the large hydrophobic surface of the A-sheet. The three N termini of the trimer are located on one end of the β barrel and these termini contain a conserved motif ([V/I]G[V/I]D[V/I]; in single-letter amino acid code) that is found in almost all of the currently known P-pant transferases [19]. This conserved stretch forms the first β strand, β1, which packs against β4 and β5 from another molecule in the trimer. Not surprisingly, the residues exposed towards the interior of this β barrel are largely hydrophobic. One of these residues, Ile5, makes extensive contacts with residues His100, Val101, Ser102, Val115, Val114 and Gln113 of the neighboring molecule. In addition, the residue in the center of strand β5, Gln113, is the only polar residue buried in the interior of the β barrel, and it makes a tight hydrogen-bonding network with the Gln113 residues from the other two molecules in the trimer. Because neither of these amino acids are directly involved in CoA or ACP binding, any effect of the mutation on AcpS activity was expected to be largely due to the packing of the trimer. Additionally, modeling showed that two molecules of the mutant AcpS would still be able to form a viable active site but that formation of the trimer would be hindered. The location of residues 2, 5 and 113 with respect to the trimerization interface can be seen in Figure 2.

Figure 5

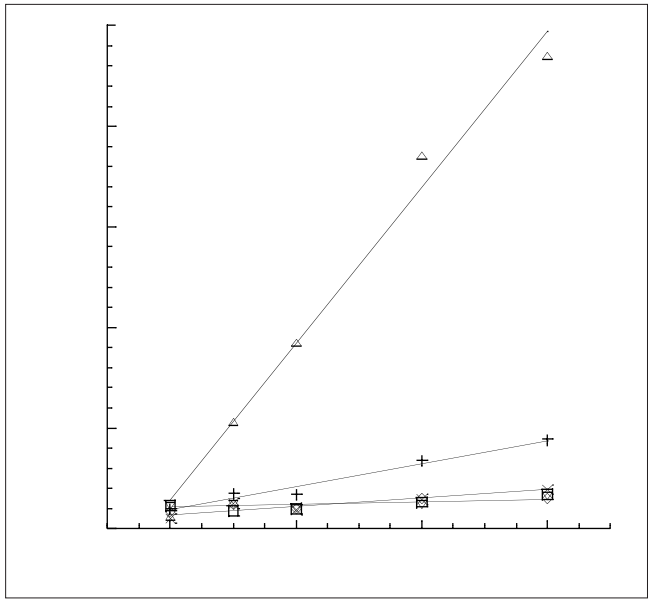

Activity measurements of wild-type (△) and mutants of AcpS. Gln113→Glu, Ile2→Ala, × Gln113→Arg, ◇ Ile5→Arg, □ and no enzyme control, ∨. [1−^{14}C]acetyl P-pant transfer assays were carried out by incubating 2 μM apo-ACP and 2 nM AcpS in 50 mM Tris-Cl pH 8.5, 200 mM NaCl, 10 mM $MgCl_2$ and 100 μM acetyl CoA at 37°C [21,29].

The mutation Gln113→Glu results in a substitution where the sidechain is of similar size but possesses a different hydrogen-bonding capacity. Additionally, a Gln113→Arg substitution was prepared so that both the size and the polarity of the sidechain were altered. We hypothesized that a non-conservative change such as Ile5→Arg would be necessary to disrupt the stable trimer structure. Finally, the AcpS construct used for obtaining the ACP–AcpS complex structure contains an Ile2→Ala mutation. Because this mutation resulted in a protein with a different retention time on the gel-filtration column, we decided to further characterize its activity.

The Ile2→Ala, Gln113→Glu, Gln113→Arg and Ile5→Arg mutant proteins were expressed in *E. coli* as soluble proteins. Except for the Ile2→Ala mutant, each showed a

reduced expression level when compared with the wild-type enzyme with the lowest level of expression observed for the Ile5→Arg mutant. We purified the mutant proteins to near homogeneity, as judged by SDS–PAGE. All of the mutants showed similar behavior to the wild-type enzyme on the ion-exchange column. The His_6-tag that was a part of the Gln113→Glu, Gln113→Arg and Ile5→Arg mutants facilitated the separation of the recombinant proteins from the endogenous *E. coli* AcpS.

The effects of these mutations on AcpS activity were investigated by measuring the AcpS catalyzed attachment of a ^{14}C-labeled acetyl-P-pant group onto apo-ACP. As shown in Figure 5, the wild-type enzyme showed an initial velocity of 30 min^{-1}, at an ACP concentration of 2 μM and a CoA concentration of 100 μM. This is comparable with previous observations for the *E. coli* AcpS [21,29]. The effect of the mutation at position 113 was highly sensitive to the nature of the substituted amino acid. The initial velocity for the Gln113→Glu mutation was approximately sevenfold slower than the wild-type enzyme, whereas the Gln113→Arg mutant was completely inactive. The Ile5→Arg mutant also proved to be inactive. Surprisingly, the Ile2→Ala mutant retained only 6% of the wild-type activity, even though the mutation is at the very N terminus of the polypeptide chain.

For the purpose of observing whether mutations hindered trimer formation, we measured their relative molecular weights as determined by mobility on a size-exclusion column under native conditions (Table 4). From the size-exclusion data, the mutants fall into two categories; those that are consistent with a trimer (wild-type-like) and those with apparently reduced molecular weight. All mutants with reduced molecular weight have no measurable activity suggesting one of three possibilities: that the trimer is necessary for activity; that the mutations have disrupted the structure of the protein around the active site; or that these single-point mutations have produced misfolded proteins. This last scenario seems unlikely as all of the mutant proteins have the same retention time on ion exchange columns. Furthermore, isotopically labeled Ile2→Ala AcpS was purified and its high-resolution NMR spectra indicated that it has a well-defined tertiary structure (GY Xu, unpublished observations). The reduced molecular weights of these mutants suggest that the wild-type trimer is the only catalytically competent form. The molecular weight of Gln113→Glu mutant is consistent with a trimer at the high concentrations used in the size-exclusion experiment. The fact that it retained some activity and its high molecular weight suggests the possibility of an alternate hydrogen-bonding network for Glu113 that allows for the formation of the trimer. This mutation could be interpreted as shifting the equilibrium away from the active trimer, resulting in reduced activity. The final mutation, Ile2→Ala, could also be interpreted in the same way, although its proximity to Asp8, one of the ligands to the metal in the active site, does not exclude local structural perturbation as a mode of inhibition.

Table 4

Gel-filtration chromatography† to estimate the apparent molecular weight of ACPS mutants.

	Retention time (min)	Apparent MW (kDa)
Standard		
Ovalbumin	16.4	44
Myoglobin	22.5	17
AcpS*		
Wild-type (His-tagged)	16.9	42
Gln113→Glu	16.5	44
Gln113→Arg	18.6	34
Ile5Arg	18.6	34
Wild-type (no tag)	17.2	41
Ile2→Ala	18.1	37

*The theoretical molecular weight of AcpS His-tagged and non His-tagged monomers are 14.8 kDa and 13.7 kDa, respectively, which are equivalent to a trimer of 44.4 kDa and 41.1 kDa. †AcpS was loaded onto a Tosohass G2000SWXL column with 50 mM NaOAc pH 4.6, 0.5 M NaCl, 10 mM $MgCl_2$ and 10 mM DTT as running buffer. These conditions were chosen because of the higher solubility of the enzyme at acidic pH. The retention time difference between the mutants and the wild-type enzyme at pH 4.6 is similar to that at lower enzyme concentration and neutral pH.

Reaction mechanism

As expected, examination of the hydrogen-bonding pattern in the AcpS–CoA structure suggests that the ζ-amino group of Lys62 has been protonated and that Asp8 has been deprotonated. It is possible that the hydrogen on Asp8 was transferred to Lys62 as they are spacially adjacent. It is tempting to speculate that one of three water molecules (Wat2) bound to the calcium is an 'activated' water owing to the short distance between it and the pyrophosphate β-phosphate. The formation of this metal-bound activated water would be in agreement with the known mechanism of other metalloenzymes in which water is utilized [30,31].

It has been suggested [22] that during the mechanistic event, it would be possible for the hydroxyl of Ser36 to replace this water molecule and be deprotonated prior to nucleophilic attack on the pyrophosphate. These structures suggest that an alternative mechanism would have the metal-bound water removing the hydroxyl hydrogen from Ser36. Examining the model of the ternary complex suggested by these structures (Figure 4) shows that with the ACP bound as shown in the ACP–AcpS costructure, a rotation of the Cα–Cβ bond would place the hydroxyl hydrogen adjacent to Wat2. Wat2 would then remove this hydrogen and prepare Ser36 for nucleophilic attack on the phosphate. Utilizing this mechanism, it is conceivable that, in the absence of substrate, the metal-bound hydroxide would be able to activate a

Figure 6

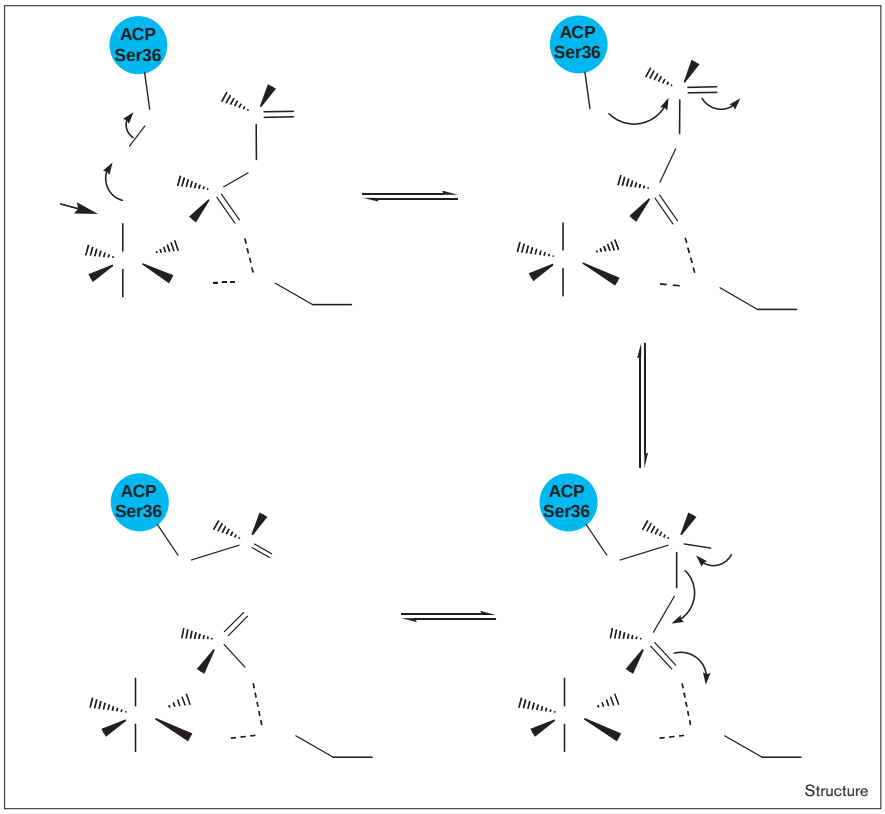

The mechanism that can be derived from the crystal structures in this study. The metal-bound water molecule removes the hydrogen from Ser36, converting it into a nucleophile and thereby initiating P-pant transfer and activation of ACP.

water molecule for nucleophilic attack of the β-phosphate of the CoA pyrophosphate. The data for the AcpS–CoA structure tends to support this hypothesis as the electron density observed for the β-phosphate (Figure 1) was seen to not properly fit the tetrahedral phosphorous placed there. If this four-coordinate tetrahedral phosphorous was replaced with a five-coordinate trigonal bi-pyramidal phosphorous it would also fit the electron density. The original MAD electron-density map and an omit map calculated for this region suggest that the best model for the β-pyrophosphate in this structure is for the CoA to be present with both a four-coordinate and a five-coordinate phosphorous.

These observations suggest a catalytic mechanism for the enzyme (Figure 6). First, Wat2 is activated by the removal of a proton. This proton could be removed by another water molecule or by Asp35 of ACP, which is spatially adjacent. Wat2 removes the hydroxyl hydrogen from Ser36 of ACP, which then carries out the nucleophilic attack on the β-phosphate of CoA. This results in the transfer of the P-pant group to Ser36, and the resulting negatively charged 3′,5′-ADP is stabilized by interactions with magnesium, Lys62 and the His105 mainchain amide. A proton can then be transferred to 3′,5′-ADP from either solvent or Lys62, followed by dissociation of the products.

This mechanism suggests that in the absence of ACP it would be possible for AcpS to catalyze the hydrolysis of CoA to 3′,5′-ADPP and phosphopantetheine. Because we observed the intact CoA moiety in the crystal structure, the equilibrium seems to favor intact CoA. Clearly, when ACP binds the equilibrium changes, resulting in the transfer of the P-pant group to ACP.

A proposed order of binding explains substrate inhibition

Preliminary studies using both gel-filtration chromatography and analytical ultracentrifugation (data not shown) on the Ile2→Ala mutant indicate an increase of the molecular weight to a trimer upon the addition of CoA. These results as well as those of prior studies [29–32] suggest that the binding of CoA to initiate the formation of a tighter protein assembly is the first event to occur. Once CoA and magnesium have bound to AcpS, the binding of ACP will initiate the P-pant transfer. This is supported by the structure as CoA bridges two monomers (Figure 2). After binding CoA, the electrostatic potentials of the binding site have changed and as ACP binds, the dipole of the ACP α3 helix is directed toward the β-phosphate of the pyrophosphate. Once the P-pant group has been transferred to ACP, the bridging and trimer stabilization function of CoA is lost. The fact that the charged phosphate that promoted ACP binding

to AcpS has now been transferred to ACP and the loss of the stability afforded to the trimer by CoA combine to facilitate the release of holo-ACP.

The ternary complex shown in Figure 4 does not have sufficient room for a CoA molecule to enter the active site if ACP binds first, so in such a case, the ACP–AcpS complex would be unproductive. This observation and hypothesis of the order of binding provides an explanation for the observation [29] that apo-ACP can be an inhibitor at higher concentrations. The model derived from these crystal structures suggests that 3′,5′-ADP would not be released until after the release of holo-ACP. It can be envisioned that if the concentration of ACP is high enough, it would be possible to trap the 3′,5′-ADP in the active site before it dissociates, again generating an unproductive complex.

Biological implications

Phosphopantetheinyl (P-pant) transferases are essential in the initiation of the biosynthesis of fatty acids, polyketide antibiotics and non-ribosomal peptides. Their function is to convert the apo-form of a carrier protein to the active holo-form by the post-translational introduction of a reactive thiol that is attached to the end of a long prosthetic group. This prosthetic group, the phosphopantetheinyl moiety of coenzyme A, is attached via a phosphodiester linkage to the hydroxymethyl sidechain of a conserved serine residue on the carrier protein. Each carrier protein has a corresponding P-pant transferase that has been optimized for its activation. Prior biochemical studies [19–34] have demonstrated that the *Escherichia coli* P-pant transferase is capable of modifying the apo-forms of several type II acyl carrier protein (ACP) homologs but shows no detectable activity towards type I P-pant-requiring proteins. Type I P-pant transferase proteins, such as Sfp and EntD, are not only active towards their type I substrates but also transfer the P-pant group onto type II apo-ACP, although only very weakly in the case of EntD [19]. This unidirectional cross-modification at first seems confusing but comparing the structure of acyl carrier protein synthase (AcpS) (subgroup II) with the structure of Sfp (subgroup I) affords an explanation. Examination of the superimposed structures show that the active site for Sfp is both more shallow and wider than the active site of holo-AcpS. This correlates well with the sizes of their substrates because the type I substrates are usually a domain of a much larger multifunctional protein. This domain can easily fit into the active site of a P-pant transferase that has a large and shallow active site such as that found in Sfp. When this domain is a part of a large protein, it cannot fit into the deep and narrow active site of a short chain P-pant transferase such as AcpS. By contrast, the smaller ACP can easily fit into the active site of AcpS as well as into the active site of Sfp-type enzymes. Modeling the ACP structure described in this article in complex with the Sfp structure from the Protein Data Bank (accession code 1QR0) shows the fit is not optimal and that the P-pant transfer should be less efficient.

Materials and methods

Expression and purification of AcpS and SeMet–AcpS

B. subtilis AcpS, cloned into pBAD/HIS, was expressed in DH10B *E. coli*. Cells were lysed in a buffer containing 50 mM HEPES-Cl, pH 7.4, 250 mM NaCl, 10 mM $MgCl_2$ and 10 mM DTT. AcpS in the soluble extract was purified on a Poros PI, Poros HS at pH 8.0, Poros HS at pH 4.5 (all from PerSeptive Biosystems, Framingham, MA), and gel-filtration chromatography steps similar to the conditions used for *E. coli* AcpS (Lambalot, 1995, Flugel, 2000). SeMet–AcpS was purified using the same procedure.

Expression and purification of ACP

B. subtilis ACP was cloned into the pGEX-6P-1 vector and expressed in *E. coli* strain BL21DE3 (pLysS). Cells were lysed in a buffer containing 50 mM Tris-Cl (pH 8.0), 300 mM NaCl, 10 mM $MgCl_2$ and 2 mM $MnCl_2$ [35]. The GST–ACP fusion protein was purified on a glutathione sepharose column (Amersham Pharmacia Biotech, Piscataway, NJ) and cleaved with Precission Protease (Amersham). ACP was purified on a MonoQ HR16/10 column (Amersham) with a NaCl gradient.

Crystallization of AcpS

Prior to crystallization, the protein was dialyzed against a solution containing 10 mM sodium acetate pH 4.4, 2 mM $MgCl_2$, 100 mM NaCl, 5 mM DTT and then concentrated to ~10 mg/ml according to the Bradford method [36]. Diffraction-quality plate-like crystals were obtained at 18°C from 2.5 M NaCl, 0.1 M Tris pH 7.0 and 0.2 M $MgCl_2$. These crystals belonged to space group $P2_1$ with cell dimensions of a = 76.26 Å, b = 76.16 Å, c = 85.69 Å, β = 93.3° and contained six molecules of AcpS in the asymmetric unit. The SeMet–AcpS also crystallized using these conditions with the exception that the concentration of DTT was increased to 10mM to help protect against oxidation of the selenium atoms.

Crystallization of AcpS with CoA

The protein solution was prepared as above with the exception that 24 h before crystallization screening, 1 mM CoA (di-sodium salt, Fluka) was added. Diffraction quality CoA–AcpS co-crystals were obtained at 18°C from 0.2 M $CaCl_2$ and 20% PEG 3350. These crystals belonged to space group R3 with cell dimensions a = b = 55.82 Å, c = 92.28 Å and contained one molecule of AcpS and one molecule of CoA in the asymmetric unit. The SeMet AcpS–CoA crystallized under the same conditions with the exception that the concentration of DTT was increased to 10 mM to help protect against oxidation of the selenium atoms.

Crystallization of AcpS with holo-ACP

Purified holo-ACP and AcpS were mixed at a 1:1.1 molar ratio and purified using a gel filtration column. The resulting purified complex was dialyzed against a solution containing 50 mM Bis-Tris pH 6.4, 100 mM NaCl, 10 mM $MgCl_2$, and 10 mM DTT before concentrating the complex to ~10 mg/ml. Crystals were grown from between 0.15 M and 0.3 M potassium formate and between 15 and 23% PEG 3350. These crystals belonged to space group $C222_1$ with unit cell parameters a = 78.46, b = 122.03, c = 136.77 Å and contained three molecules of AcpS and three molecules of ACP in the asymmetric unit.

Data collection: native

Single-wavelength (1.2 Å) data for the native AcpS and AcpS–CoA crystals were collected on beamline 5.0.2 at the ALS, Berkeley using an ADSC Quantum-4 CCD detector. A single crystal, cooled to −180°C, was used for each data set. The data were processed using DENZO and Scalepack [37] and the statistics from refinement are given in Table 2.

Data from the ACP–AcpS complex crystals were collected using a R-Axis IV mounted on a Rigaku RUH2R rotating anode operating at 5 kW from a

single crystal, cooled to −180°C. The oscillation images were processed as described above with the statistics also reported in Table 1.

Data collection: MAD

During the same trip, MAD data were collected on beamline X12-C at the NSLS (Brookhaven National Laboratory, Upton, NY) from a single crystal of SeMet–AcpS, $P2_1$ form and from a single crystal of the SeMet-AcpS–CoA complex, R3 form. Each crystal was cooled to −180°C for data collection as described above. The wavelengths used can be found in Table 1. These data were then used as input to the program SOLVE [38] for local scaling of the datasets of the Selenium atom positions. Heavy atom parameters for each were refined with SHARP [39].

Model building and refinement: AcpS

The structure of the AcpS monoclinic form was built into the original 2.5 Å resolution solvent-flattened symmetry-averaged MAD map using the X-AUTOFIT features within QUANTA (Molecular Simulations Inc., San Diego, CA). The phases were then extended from 2.5–2.2 Å with symmetry averaging in DM. This model was then used as the initial model for refinement using the program CNS [40] against the native data, which extended to 1.8 Å. Prior to refinement, 5% of the data were randomly selected and designated as a R_{free} test set to monitor the progress of the refinement. Following seven cycles of refining and rebuilding the refinement converged with a model which contained six molecules of AcpS, 471 water molecules, eight sodium ions, 19 chlorine ions, five DTT molecules and two glycerol molecules at an R_{cryst} of 19.6% (R_{free} 21.9%). The refinement statistics are given in Table 2.

Model building and refinement: AcpS–CoA

The structure the AcpS–CoA complex was solved using a combination of molecular replacement and MAD phasing. Monomer 1 of the monoclinic AcpS structure was utilized as a molecular replacement probe with AMoRe [24]. The molecular replacement solution was then rebuilt into a 2.1 Å resolution solvent-averaged MAD map thus eliminating any bias from the molecular replacement solution. The structure was refined in CNS using the methods described above. Refinement converged after six rebuilding cycles with a R_{cryst} of 18.5% and a R_{free} of 20.1%. The final model consisted of residues 1–118, CoA, 99 waters, two calcium ions and one chloride ion. The refinement statistics are given in Table 2.

Model building and refinement: AcpS–holo-ACP

The complex between holo-ACP and AcpS was generated from protein purified by gel filtration thus generating a stoichiometric ratio. Crystals of this complex diffract to 2.3 Å using an R-Axis IV mounted on a Rigaku RUH2R rotating anode operating at 5 kW. The structure of the ACP–AcpS complex was solved by molecular replacement using the program AMoRe [24], with the trimer of AcpS as found in the AcpS–CoA structure as the probe. Prior to refinement, 10% of the data were randomly selected and designated as a R_{free} test set to monitor the progress of the refinement. The structure of the AcpS trimer was then rebuilt within QUANTA utilizing a series of omit maps. During this rebuilding, extra density was found in each active site that sharpened after each cycle of rebuilding. When the AcpS molecules had been rebuilt, the NMR structure of the *B. subtilis* ACP (Guang-Yi Xu, manuscript in preparation) was rotated into the density found in the active site. As a result of a large domain shift, a consequence of binding to AcpS, there were enough differences between the NMR structure and the X-ray data to preclude using the NMR model as the starting point for refinement. Instead, the location of Met44 was noted from the NMR structure and the remainder of the ACP molecule was built into density using omit maps from that residue. Reference to the NMR structure as a source of secondary structure information allowed the structure of the three ACP molecules to be built into the electron density rapidly.

When roughly 80% of the ACP had been built into density, that ACP–AcpS model was then used as the initial model for refinement using CNS. Following six cycles of refining and rebuilding the refinement converged with a model that contained three molecules of AcpS, three molecules of AcpS and 117 solvent molecules at an R_{cryst} of 22.2% and R_{free} of 27.9%. The refinement statistics are shown in Table 2.

Accession numbers

The coordinates for the three structures described in this paper have been deposited in the PDB. The PDB ID codes are 1F7T for the AcpS structure, 1F7L for the AcpS–CoA structure and 1F80 for the AcpS–holo-ACP structure.

Acknowledgements

We are indebted to Guang-Yi Xu for allowing us access to the coordinates of the NMR structure of ACP and for communicating the unpublished NMR data regarding the Ile2→Ala AcpS mutant. We also thank Karl Malakian and Michelle Catino for the AcpS and ACP grown in *E. coli*. We are also grateful to Ann Aulabaugh for her work on characterizing the AcpS system using sedimentation equilibrium analysis. We are most thankful to Thomas Earnest and the Advanced Light Source 5.0.2 Beamline group, as well as Bob Sweet and the X12-C personnel at the NSLS for assistance with data collection. We are also grateful to Francis Sullivan and Saurabh Menon for their help in proofreading the manuscript and their valuable suggestions.

References

1. Magnuson, K., Jackowski, S., Rock, C.O. & Cronan, J.E. Jr. (1993). Regulation of fatty acid biosynthesis in *Escherichia coli*. *Microbiol. Rev.* **57**, 522-542.
2. Lynen, F. (1980). On the structure of fatty acid synthetase of yeast. *Eur. J. Biochem.* **112**, 431-442.
3. Wakil, S.J., Stoops, J.K. & Joshi, V.C. (1983). Fatty acid synthesis and its regulation. *Annu. Rev. Biochem.* **52**, 537-579.
4. Shen, B., Summers, R.G., Gramajo, H., Bibb, M.J. & Hutchinson, C.R. (1992). Purification and characterization of the acyl carrier protein of the *Streptomyces glaucescens* tetracenomycin C polyketide synthase. *J. Bacteriol.* **174**, 3818-3821.
5. Hopwood, D.A. & Sherman, D.H. (1990). Molecular genetics of polyketides and its comparison to fatty acid biosynthesis. *Annu. Rev. Genet.* **24**, 37-66.
6. Kleinkauf, H. & Von Dohren, H. (1996). A nonribosomal system of peptide biosynthesis. *Eur. J. Biochem.* **236**, 335-351.
7. Marahiel, M.A. (1992). Multidomain enzymes involved in peptide synthesis. *FEBS Lett.* **307**, 40-43.
8. White, R.H. (1980). Stoichiometry and stereochemistry of deuterium incorporated into fatty acids by cells of *Escherichia coli* grown on [methyl-$^2H^3$]acetate. *Biochemistry* **19,** 9-15.
9. Sanyal, I., Lee, S.-L. & Flint, D.H. (1994). Biosynthesis of pimeloyl-CoA, a biotin precursor in *Escherichia coli*, follows a modified fatty acid synthesis pathway: ^{13}C-labeling studies. *J. Am. Chem. Soc.* **116**, 2637-2638.
10. Rawlings, M. & Cronan, J.E.J. (1988). *Escherichia coli* acyl carrier protein. *FASEB J.* **2**, A1559.
11. Hill, R.B., MacKenzie, K.R., Flanagan, J.M., Cronan, J.E.J. & Prestegard, J.H. (1995). Overexpression, purification, and characterization of *Escherichia coli* acyl carrier protein and two mutant proteins. *Protein Expr. Purif.* **6**, 394-400.
12. Rock, C.O. & Cronan, J.E.J. (1980). Improved purification of acyl carrier protein. *Anal. Biochem.* **102**, 362-364.
13. Holak, T.A., Nilges, M., Prestegard, J.H., Gronenborn, A.M. & Clore, G.M. (1988). Three-dimensional structure of acyl carrier protein in solution determined by nuclear magnetic resonance and the combined use of dynamical simulated annealing and distance geometry. *Eur. J. Biochem.* **175**, 9-15.
14. Furukawa, H., Tsay, J.T., Jackowski, S., Takamura, Y. & Rock, C.O. (1993). Thiolactomycin resistance in *Escherichia coli* is associated with the multidrug resistance efflux pump encoded by emrAB. *J. Bacteriol.* **175**, 3723-3729.
15. Bergler, H., *et al.*, & Turnowsky, F. (1994). Protein EnvM is the NADH-dependent enoyl-ACP Reductase (FabI) of *Escherichia coli*. *J. Biol. Chem.* **269**, 5493-5496.
16. Banerjee, A., *et al.*, & Jacobs, W.R. Jr. (1994). inhA, a gene encoding a target for isoniazid and ethionamide in *Mycobacterium tuberculosis*. *Science* **263**, 227-230.
17. Dessen, A., Quémard, A., Blanchard, J.S., Jacobs, W.R., Jr. & Sacchettini, J.C. (1995). Crystal structure and function of the isoniazid target of *Mycobacterium tuberculosis*. *Science* **267**,1638-1641.
18. Quémard, A., *et al.*, & Blanchard, J.S. (1995). Enzymatic characterization of the target for isoniazid in *Mycobacterium tuberculosis*. *Biochemistry* **34**, 8235-8241.

19. Lambalot, R.H., *et al.*, & Walsh, C.T. (1996). A new enzyme superfamily – the phosphopantetheinyl transferases. *Chem. Biol.* **3**, 923-936.
20. Elovson, J. & Vagelos, P.R. (1968). Acyl carrier protein X. acyl carrier protein synthetase. *J. Biol. Chem.* **243**, 3603-3611.
21. Lambalot, R.H. & Walsh, C.T. (1995). Cloning, overproduction, and characterization of the *Escherichia coli* holo-acyl carrier protein synthase. *J. Biol. Chem.* **270**, 24658-24661.
22. Reuter, K., Mofid, M.R., Marahiel, M.A. & Ficner, R. (1999). Crystal structure of the surfactin synthetase-activating enzyme Sfp: a prototype of the 4′-phosphopantetheinyl transferase superfamily. *EMBO J.* **18**, 6823-6831.
23. Hendrickson, W.A. (1991). Determination of macromolecular structures from anomalous diffraction of synchrotron radiation. *Science* **254**, 51-58.
24. Navaza, J. (1994). AMoRe: an automated package for molecular replacement. *Acta Crystallogr. A* **50**, 157-163.
25. Hirel, P.H., Schmitter, M.J., Dessen, P., Fayat, G. & Blanquet, S. (1989). Extent of N-terminal methionine excision from *Escherichia coli* proteins is governed by the side-chain length of the penultimate amino acid. *Proc. Natl Acad. Sci. USA* **86**, 8247-8251.
26. Holm, L. & Sander, C. (1993). Protein structure comparison by alignment of distance matrices. *J. Mol. Biol.* **233**, 123-138.
27. Clements, A., Rojas, J.R., Trievel, R.C., Wang, L., Berger, S.L. & Marmorstein, R. (1999). Crystal structure of the histone acetyltransferase domain of the human PCAF transcriptional regulator bound to coenzyme A. *EMBO J.* **18**, 3521-3532.
28. Lambalot, R.H. & Walsh, C.T. (1997). Holo-[acyl-carrier-protein] synthase of *Escherichia coli*. *Methods Enzymol.* **279**, 254-262.
29. Flugel, R.S., Hwangbo, Y., Lambalot, R.H., Cronan, J., J. E. & Walsh, C.T. (2000). Holo-(acyl carrier protein) synthase and phosphopantetheinyl transfer in *Escherichia coli*. *J. Biol. Chem.* **275**, 959-968.
30. Fabiane, S.M., *et al.*, Sutton, B.J. (1998). Crystal structure of the zinc-dependent β-lactamase from *Bacillus cereus* at 1.9 Å resolution: binuclear active site with features of a mononuclear enzyme. *Biochemistry* **37**, 12404-12411.
31. Lin, J., Abeygunawardana, C., Frick, D.N., Bessman, M.M. & Mildvan, A.S. (1997). Solution structure of the quaternary mutt-M^{2+}-AmpcpP-M^{2+} complex and mechanism of its pyrophosphohydrolase action. *Biochemistry* **36**, 1199-1211.
32. Polacco, M.L. & Cronan, J., J.E. (1981). A mutant of *Escherichia coli* conditionally defective in the synthesis of holo-[acyl carrier protein]. *J. Biol. Chem.* **256**, 5750-5754.
33. Ritsema, T., Geiger, O., van Dillewijn, P., Lugtenberg, B.J.J. & Spaink, H.P. (1994). Serine residue 45 of nodulation protein NodF from *Rhizobium leguminosarum bv. viciae* is essential for its biological function. *J. Bacteriol* **176**, 7740-7743.
34. Debabov, D.V., Heaton, M.P., Zhang, Q., Stewart, K.D., Lambalot, R.H. & Neuhaus, F.C. (1996). The D-alanyl carrier protein in *Lactobacillus casei*: cloning, sequencing, and expression of dltC. *J. Bacteriol.* **178**, 3869-3876.
35. Fischl, A.S. & Kennedy, E.P. (1990). Isolation and properties of acyl carrier protein phosphodiesterase of *Escherichia coli*. *J. Bacteriol.* **172**, 5445-5449.
36. Bradford, M. (1976). A rapid and sensitive method for the quantitation of microgram quantities of protein utilizing the principle of protein-dye binding. *Anal. Biochem.* **72**, 248-254.
37. Otwinowski, Z. & Minor, W. (1997). Processing of X-ray diffraction data collected in oscillation mode. *Methods Enzymol.* **276**, 307-326.
38. Terwilliger, T.C. & Berendzen., J. (1999). Automated structure solution for MIR and MAD. *Acta Crystallogr. D* **55**, 849-861.
39. de La Fortelle, E. & Bricogne, G. (1997). Maximum-likelihood heavy-atom parameter refinement in the MIR and MAD methods. *Methods Enzymol.* **276**, 472-494.
40. Brünger, A.T., *et al.*, & Warren, G.L. (1998). Crystallography & NMR system: a new software suite for macromolecular structure determination. *Acta Crystallogr. D* **54**, 905-921.
41. Carson, M. (1997). Ribbons. *Methods Enzymol.* **277**, 493-505.
42. Nicholls, A., Sharp, K.A. & Honig, B. (1991). Protein folding and association: insights from the interfacial and thermodynamic properties of hydrocarbons. *Proteins* **11**, 281-296.

Because *Structure with Folding & Design* operates a 'Continuous Publication System' for Research Papers, this paper has been published on the internet before being printed (accessed from http://biomednet.com/cbiology/str). For further information, see the explanation on the contents page.